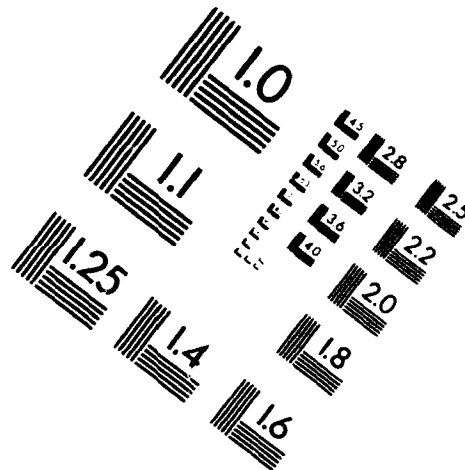# AIIM

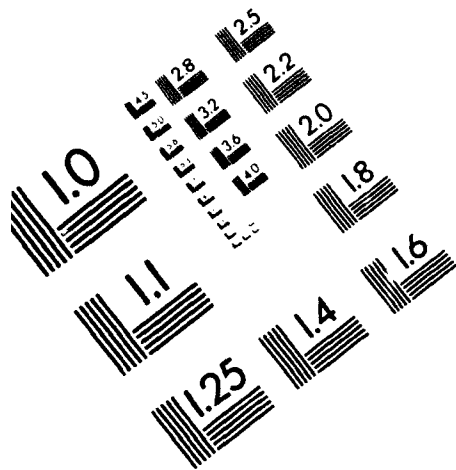**Association for Information and Image Management**

1100 Wayne Avenue, Suite 1100
Silver Spring, Maryland 20910

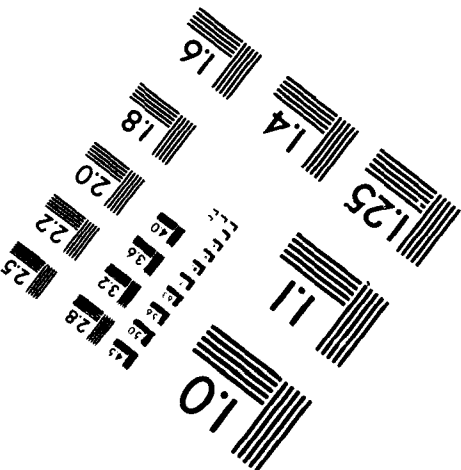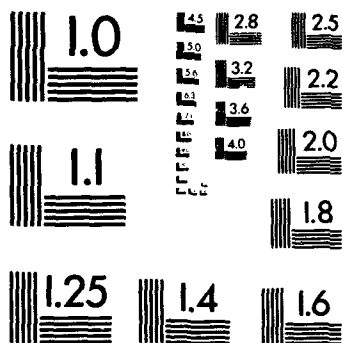301/587-8202

Centimeter

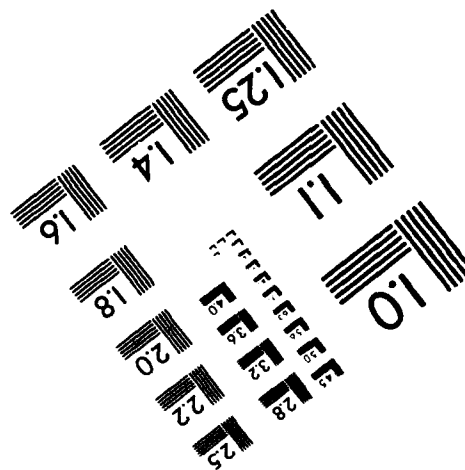1 2 3 4 5 6 7 8 9 10 11 12 13 14 15 mm

Inches

1.0

1.1

1.25

1.4

1.6

MANUFACTURED TO AIIM STANDARDS
BY APPLIED IMAGE, INC.

SMC-TR-93-42

AD-A270 598

Acoustic Microscopy and Nonlinear Effects in Pressurized Superfluid Helium

31 August 1993

Prepared by

A. A. MOULTHROP, M. S. MUHA, G. C. KOZLOWSKI,
and C. P. SILVA
Communications Systems Subdivision
Electronics and Sensors Division
The Aerospace Corporation

and

B. HADIMIOGLU
Edward L. Ginzton Laboratory
Stanford University, Stanford, CA 94305

DTIC
ELECTE
OCT 12 1993
S **A** **D**

Prepared for

SPACE AND MISSILE SYSTEMS CENTER
AIR FORCE MATERIEL COMMAND
2430 E. El Segundo Boulevard
Los Angeles Air Force Base, CA 90245

Engineering and Technology Group

**THE AEROSPACE
CORPORATION**
Segundo, California

93 10 8 121

WM KYLE SNEDDON, Capt, USAF
Deputy Chief, Industrial & Int'l Div

REPORT DOCUMENTATION PAGE

a. REPORT SECURITY CLASSICATION	1b. RESTRICTIVE MARKINGS
Unclassified	

2a. SECURITY CLASSIFICATION AUTHORITY	3. DISTRIBUTION/AVAILABILITY OF REPORT
2b. DECLASSIFICATION/DOWNGRADING SCHEDULE	Approved for public release; distribution unlimited.

4. PERFORMING ORGANIZATION REPORT NUMBER(S)	5. MONITORING ORGANIZATION REPORT NUMBER(S)
TR-0091(6925-02)-1	SMC-TR-93-42

6a. NAME OF PERFORMING ORGANIZATION	6b. OFFICE SYMBOL (If applicable)	7a. NAME OF MONITORING ORGANIZATION
The Aerospace Corporation Communications Systems Subdivision		Space and Missile Systems Center

6c. ADDRESS (City, State, and ZIP Code)	7b. ADDRESS (City, State, and ZIP Code)
El Segundo, CA 90245	Los Angeles Air Force Base Los Angeles, CA 90009-2960

8a. NAME OF FUNDING/SPONSORING ORGANIZATION	8b. OFFICE SYMBOL (If applicable)	9. PROCUREMENT INSTRUMENT IDENTIFICATION NUMBER
		F04701-88-C-0089

8c. ADDRESS (City, State, and ZIP Code)	10. SOURCE OF FUNDING NUMBERS			
	PROGRAM ELEMENT NO.	PROJECT NO.	TASK NO.	WORK UNIT ACCESSION NO.

11. TITLE (Including Security Classification)
Acoustic Microscopy and Nonlinear Effects in Pressurized Superfluid Helium

12. PERSONAL AUTHOR(S) Moulthrop, A. A.; Muha, M. S.; Kozlowski, G. C.; Silva, C. P.; Hadimioglu, B.

13a. TYPE OF REPORT	13b. TIME COVERED FROM _____ TO _____	14. DATE OF REPORT (Year, Month, Day) 31 August 1993	15. PAGE COUNT 30

16. SUPPLEMENTARY NOTATION

17. COSATI CODES			18. SUBJECT TERMS (Continue on reverse if necessary and identify by block number)
FIELD	GROUP	SUB-GROUP	Cryogenic microscopy, Harmonic generation, Nonlinear acoustics

18. ABSTRACT (Continue on reverse if necessary and identify by block number)

The operation of an acoustic microscope having a resolution of 15 nm has been demonstrated. It uses as a coupling medium superfluid ^{4}He colder than 0.9 K and pressurized to greater than 20 bar. The microscope is now being used to image objects that show little or no contrast on a scanning electron microscope. In addition, the acoustic microscope is being used to study the properties of sound propagation in the coupling fluid. At low acoustic intensities, the coupling fluid has very low acoustic attenuation at the microscope's operating frequency (15.3 GHz), but near the focal point the acoustic intensity can be high enough that the helium behaves with extreme nonlinearity. In fact, this medium is capable of entering new regimes of nonlinear interaction. Plots of the received signal versus input power display a nearly complete pump depletion at certain input power levels and a reconversion to the pump frequency at higher power levels. Such behavior has never before been observed. We present arguments that the process underlying this nonlinear behavior is harmonic generation.

20. DISTRIBUTION/AVAILABILITY OF ABSTRACT	21. ABSTRACT SECURITY CLASSIFICATION
[X] UNCLASSIFIED/UNLIMITED ☐ SAME AS RPT. ☐ DTIC USERS	Unclassified

22a. NAME OF RESPONSIBLE INDIVIDUAL	22b. TELEPHONE (Include Area Code)	22c. OFFICE SYMBOL

DD FORM 1473, 84 MAR 83 APR edition may be used until exhausted. All other editions are obsolete.

SECURITY CLASSIFICATION OF THIS PAGE
UNCLASSIFIED

Preface

This report is an expanded version of the article of the same title published in *IEEE Transactions on Ultrasonics, Ferroelectrics, and Frequency Control*, Vol. 39, No. 2 (March 1992), pp. 204-211.

Acknowledgments

Contents

Figures

1. Introduction

Superfluid ^{4}He is a unique fluid for ultrasonics. Of all known fluids, it has the lowest ultrasonic attenuation and, because it has a low speed of sound, possibly the lowest power density for the onset of nonlinear effects. This low attenuation makes superfluid helium the most suitable coupling fluid for high-resolution acoustic microscopy. Because acoustic microscopes are generally diffraction limited, a shorter wavelength corresponds to a higher resolution. Thus the low sound speed is an added advantage, since a wave of given frequency has a shorter wavelength in superfluid helium than in other fluids. The low power density for the onset of nonlinearity is a disadvantage for acoustic microscopy, since it limits the received signal; however, it does present a unique opportunity to study ultrasonic wave propagation that is highly nonlinear.

The first successful cryogenic acoustic microscope [1] operated at a frequency of 4.2 GHz and had a resolution of about 40 nm. Later, its operating frequency was increased to 8 GHz with a correspondingly better resolution of 20 nm [2]. To eliminate the acoustic attenuation in the coupling fluid, both of these instruments used unpressurized superfluid helium at temperatures in the 100-mK range as a coupling fluid for the ultrasonic waves. A cumbersome and expensive ^{3}He-^{4}He dilution refrigerator is required to achieve and maintain temperatures in this low range. It is possible, however, to achieve negligible losses in the helium coupling fluid at temperatures as high as 0.9 K by pressurizing the liquid helium to 20 bar. At this temperature, a much simpler to operate and less expensive ^{3}He cryostat is sufficient. The instrument reported here is the first *high-resolution* acoustic microscope to operate in pressurized superfluid helium. It operates at a frequency of 15.3 GHz and has a resolution of 15 nm. Another research group has also operated an acoustic microscope in pressurized superfluid helium [3], but at the much lower frequency of 380 MHz. At this frequency their instrument had a resolution of 0.6 μm, comparable to that of acoustic microscopes that use water as the coupling fluid.

Operating at high resolution in pressurized superfluid helium has enabled us to observe a new nonlinear ultrasonic effect. We have observed nearly complete pump depletion at certain input power levels and a startling reconversion to the pump frequency at higher power levels. Many other investigators have observed pump depletion [4,5], but none has ever observed reconversion to the pump frequency at higher power levels. Furthermore, this phenomenon has never been theoretically predicted. Below, we review previous theoretical work as well as propose extensions to this work that should explain the observed effect.

5

2. Experimental Apparatus

The heart of the acoustic microscope is a c-axis-oriented sapphire rod having an acoustic transducer on one end and an acoustic lens on the other (see Fig. 1). The acoustic lens element is a polished spherical depression ground on one end of the sapphire rod. A 40-nm-thick layer of molybdenum and an 80-nm-thick layer of amorphous carbon are both evaporated on the lens surface, serving as matching layers to reduce the large acoustic-impedance mismatch between sapphire and liquid helium. The acoustic transducer is a multilayer ZnO piezoelectric thin film [6]. Each layer is 170 nm thick, and the crystal orientation of alternate layers is varied to attain periodic coefficients of piezoelectric coupling. This type of multilayer transducer presents a higher impedance to the incoming microwave pulses, resulting in a better match and a higher conversion efficiency than would be possible at 15.3 GHz with the single-layer transducers used on lower-frequency microscopes [2]. The measured one-way conversion loss of the multilayer transducer at 77 K is 15 dB.
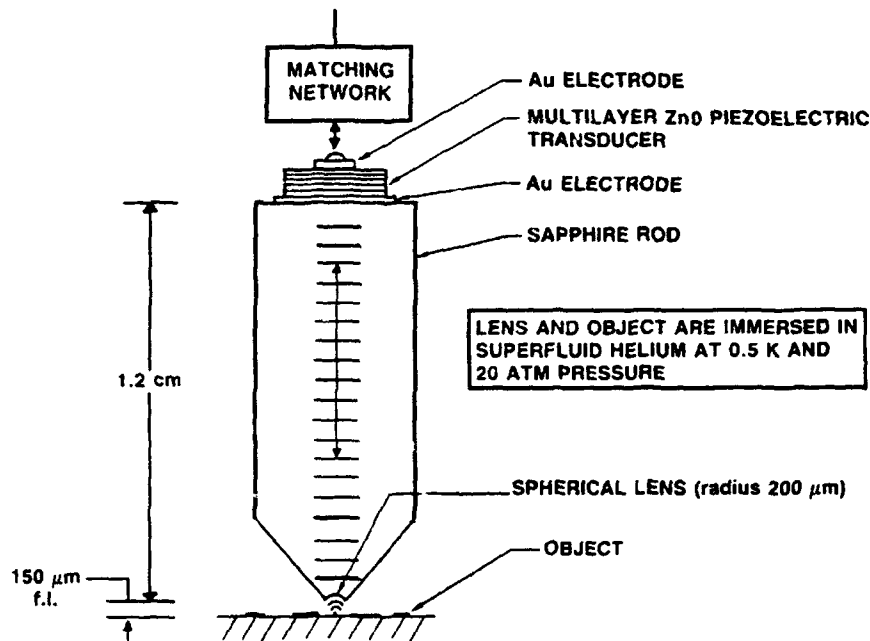
Fig. 1. Cross-sectional view of the 15.3-GHz acoustic lens.

The block diagram of the system is shown in Fig. 2. This reflection-type acoustic microscope uses 700-ns-wide pulses, and a superheterodyne receiver with amplitude detection. The pulses are repeated at a rate consistent with both the computer-controlled data-acquisition system and a mechanical raster scan of the lens across the object. The raster scan is accomplished by means of two piezoflex stages [7] stacked at right angles. Each piezoflex stage is a multiple lever-arm arrangement that multiplies the motion of a piezoelectric stack (see Fig. 3). Each piezoelectric stack moves 1 μm at liquid helium temperatures, and the output member of its piezoflex stage moves 15 μm. The piezoelectric stack is inserted loosely into the piezoflex stage at room temperature, and the piezoflex stage, being made of stainless steel, contracts more than the piezoelectric stack on cooling, putting a compressive load on the stack.

7
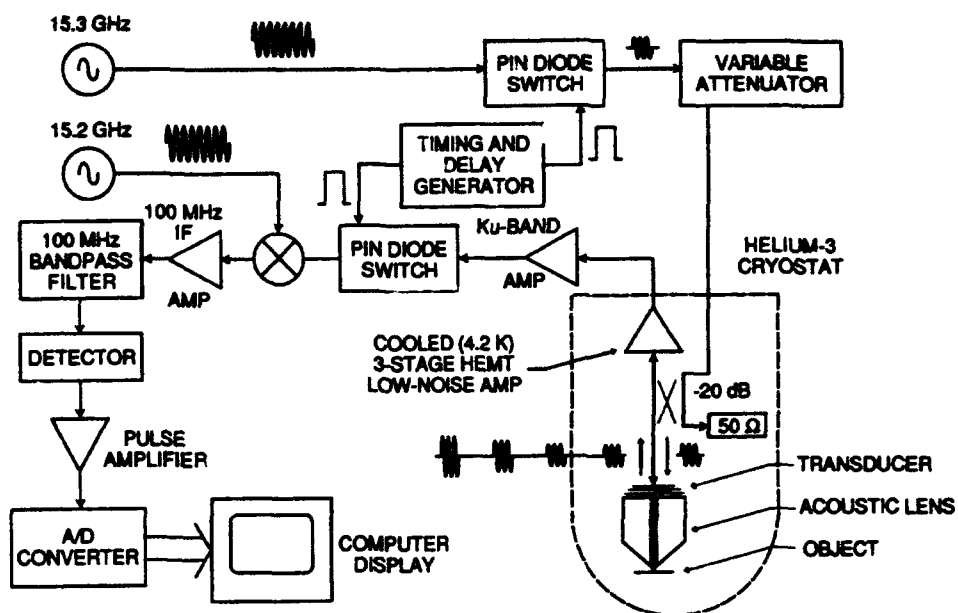
Fig. 2. Block diagram of the 15.3-GHz cryogenic acoustic microscope.
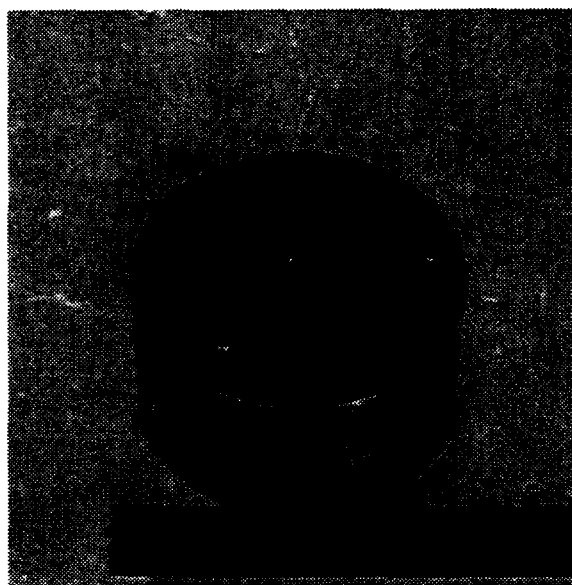
Fig. 3.   Piezoflex scanning stages. The piezoelectric actuating elements are located in the dark rectangular region.

The object is brought into focus by means of a stepper motor coupled to a harmonic-drive gear [8] whose rotary motion is converted to linear motion by a screw. The stepper motor is a commercial motor rewound with superconducting wire, and has been mechanically modified for cryogenic use as previously described [9]. The harmonic-drive gear is a compact, pancake-type gear, with a bronze separator between the ball bearings replacing the usual plastic separator. The bronze separator provides a better match in thermal contraction to the other materials used (e.g. steel) than plastic, so there is less tendency to bind. To reduce vibration, the screw is kept under tension by means of a flat spring that has a higher resonant frequency in the horizontal plane than in the vertical, or focusing, direction (see Fig. 4). All the bearings and other sliding surfaces are lubricated with molybdenum disulfide. A gold-covered alumina substrate is attached to the sample stage to serve as a capacitor plate, with the opposite capacitor plate attached to the lens; both plates are in a plane perpendicular to the optical axis of the microscope. The focusing motion is then sensed by measuring the change in capacitance between the two plates by means of an ac capacitance bridge. Coarse positioning of the sample is achieved by mounting the sample on a magnet and pulsing superconducting coils situated under a smooth substrate on which the magnet sits (see Fig. 5).

A crucial consideration in the design of this acoustic microscope was the thermal loading on the ^{3}He cryostat. The ^{3}He cryostat is less expensive and simpler to operate than a dilution refrigerator, but its refrigeration capability is lower, especially because it cannot refrigerate continuously but only operates in a single-shot mode. Hence the heat capacity of the sample cell must be kept to a minimum. The heat capacity of the sample cell between the pumped ^{4}He temperature of 1.3 K and the ^{3}He temperature of 0.5 K is dominated by the ^{4}He liquid. Hence the volume in the sample cell occupied by the ^{4}He must be kept to a minimum, that is, the positioning hardware must be tightly packed with very little free volume. Our sample cell contains about 50 cm^3 of liquid ^{4}He.
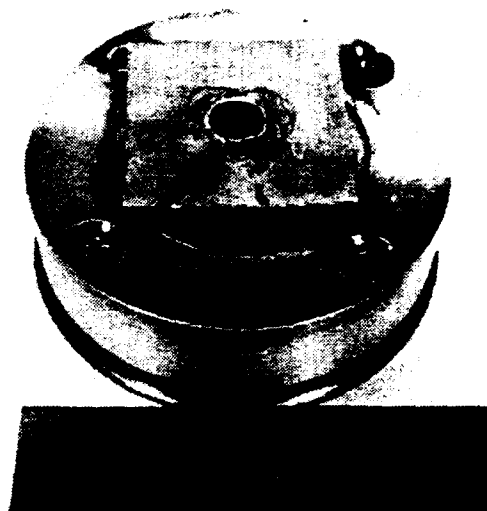

Fig. 4. An early version of the rigid sample stage. Note the flat spring ("spider") that allows the coarse focusing movement. Also shown is one of the capacitor plates used in the vertical position sensor.
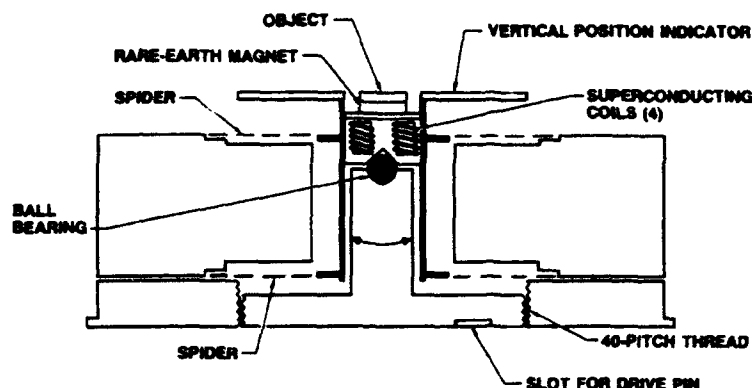
Fig. 5. Cross-sectional view of the sample stage and coarse positioning system. It provides the coarse-focusing motion in 0.1–μm increments and coarse x-y sample positioning.

Another consideration is the heat dissipation of the positioning system. The superconducting stepper motor dissipates about 2 mW in operation, and all other positioning hardware dissipates less than 1 mW in operation. The thermal conductivity of the large number of electrical leads required to operate the sample positioning and focusing mechanisms must be considered also. To minimize the heat conducted to the sample cell, all wiring from the sample cell is composed of 0.076-mm-thick niobium-titanium (Nb-Ti) alloy clad with a 0.025-mm-thick layer of copper and insulated with Formvar [10]. This wiring is thermally anchored at 1 K, from which it connects to standard 34 SWG copper wire that continues to connectors at the top of the cryostat. The copper cladding allows for room-temperature testing of the positioning hardware without imposing too great a heat load on the cryostat.

A stainless-steel capillary (having a 0.55-mm outer diameter and a 0.13-mm wall thickness) is used to supply He^4 to the microscope. This capillary is thermally anchored at 1 K. Since the capillary is small and stainless steel is a poor thermal conductor, the resulting heat load on the sample cell is small.

Another possible thermal leakage path to the sample cell is the coaxial cable that carries the microwave signal between the directional coupler (at 4 K) and the acoustic lens. To minimize thermal conductivity, superconducting cable having a 2.16-mm-diameter lead (Pb) outer conductor and a Nb center conductor is used [11]. SMA-type connectors cannot be used on this cable, because they do not have a captivated center pin; repeated thermal cycling in the cryostat causes the center pin to creep into the cable and detach itself from its mating connector. To overcome this problem, a Wiltron K-connector having a captivated center pin was used [12].

A high-resolution microscope such as this one must be designed to minimize mechanical vibrations of the sample and lens that could blur the images. Vibration amplitudes can be minimized by increasing the rigidity of the support structure and decreasing its mass, to increase the resonant frequencies of any mechanical modes. This is effective because most of the energy in building and machine vibrations is in the frequency range from 10 to 100 Hz. In addition, the whole cryostat is suspended from an optical table. The single required high-pumping-rate hose is fed through a vi-

10

bration-isolated ballast, while the other pumping lines are coupled to the cryostat through flexible small-diameter tubing.

3. Results

The received signal at constant input power is shown as a function of temperature in Fig. 6. This demonstrates that cooling the microscope substantially below 0.9 K does not increase the signal. In view of this, we operate the microscope between 0.3 and 0.5 K, where no temperature dependence of the signal is seen. However, the signal decreases dramatically as the temperature is increased above 0.9 K, unquestionably because the attenuation in the superfluid ^{4}He increases. Because the dominant excitations present in the fluid above 0.9 K are rotons [13], phonon-roton scattering is probably responsible for the increased attenuation in this temperature range.
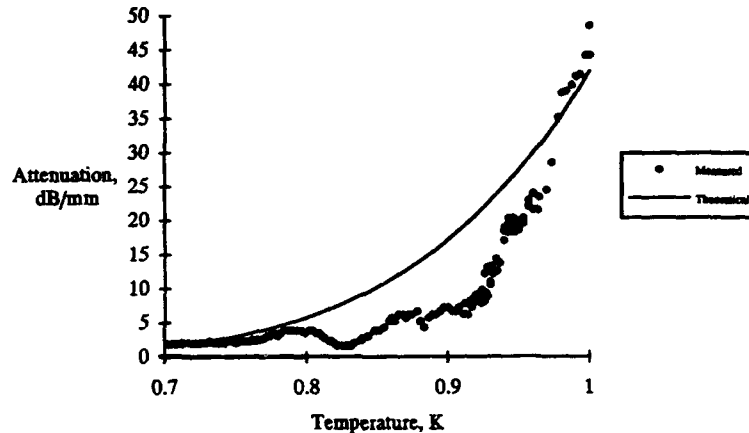
Fig. 6. Temperature dependence of the received signal. The input power was -17.5 dBm at the transducer and the pressure in the superfluid helium was 21.5 bar.

The theoretical curve in Fig. 6 comes from assuming that the attenuation is proportional to the product of the density of rotons (derived from the Landau model [13]) and their scattering cross section, taken to be 4.4×10^{-8} cm^2. To plot the experimental data it was necessary to use an arbitrary multiplicative constant, chosen to fit the theoretical expectation that the attenuation should be low when it is nearly independent of temperature. Even with these arbitrary constants, the agreement between theory and measurement is poor, indicating that processes other than simple scattering from rotons may be occurring.

As mentioned above, the received signal as a function of input power displays an oscillatory behavior, as shown in Fig. 7. These data were taken with the sample-to-lens distance held constant as the input power was increased. The oscillations in the received signal versus input power indicate the presence of a coherent energy-exchange process (e.g. a coupled harmonic oscillator that can exchange its energy between two modes), rather than an incoherent, dissipative process. In other fluids (e.g. water) this coherent process may also be present, but it is probably dominated by dissipation that increases as the square of the frequency. In unpressurized superfluid helium below a temperature of about 100 mK, the dissipation is low, and the three-phonon process of spontaneous decay is the mechanism for pump depletion [5]. The oscillatory behavior of the received signal versus input power that we observe has not been seen in unpressurized superfluid helium, so apparently spontaneous decay is not the process responsible for this behavior. In pressurized superfluid helium, spontaneous decay and all other three-phonon processes are forbidden. Hence the observed behavior must be the result of either a four-phonon process or harmonic generation. Harmonic gen-

13

eration is a strong process that can be reversible in the non-phase-matched case. Below we investigate the possibility that harmonic generation is occurring.

If the distance between the lens and the sample is not fixed, but rather is adjusted at each input power level for maximum received signal, and if received signal is again plotted against input power, a different curve results (Fig. 8). A comparison of Fig. 7 with Fig. 8 illustrates that the position of best focus varies with input power, a result that is not predicted by classical optics. If the focus position were not a function of input power, the two curves would be identical.

At low input power, where the ultrasonic propagation in the liquid helium is linear, the images we obtained have a diffraction-limited resolution of 15 nm. This is exactly what is predicted by the use

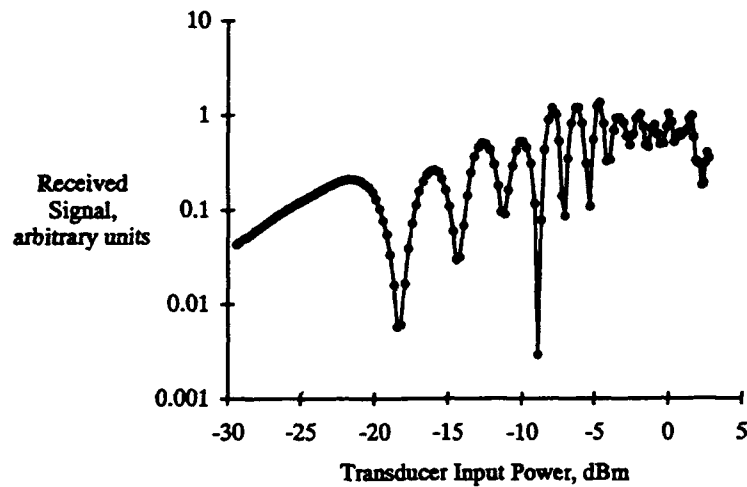*Fig. 7. Plot of the received signal vs. transducer input power. Periodic depletion and reconversion to the fundamental are evident above a transducer input power of -20 dBm. The lens-to-sample distance was held constant for this measurement.*
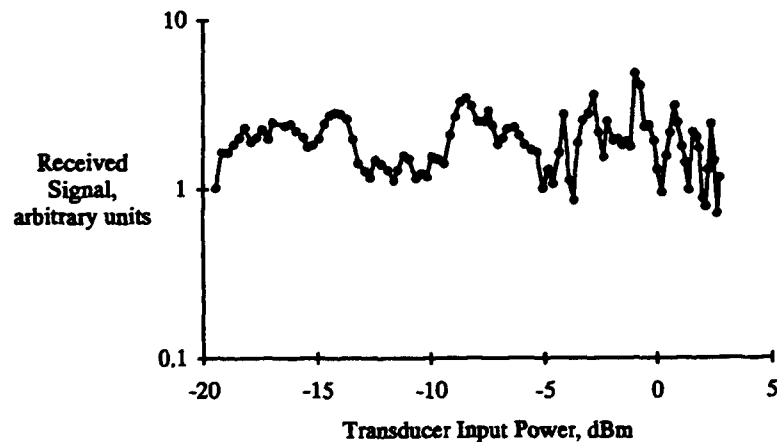

Fig. 8. Plot of the received signal vs. transducer input power. The lens-to-sample distance was varied to maximize the received signal for each power step.
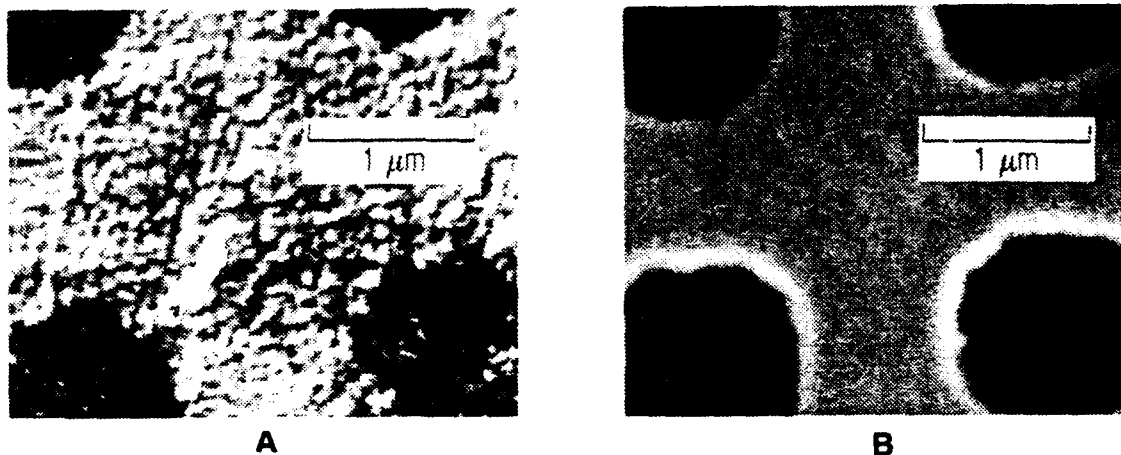
14

A   **B**

*Fig. 9(a,b).   Acoustic (a) and SEM (b) images of similar areas of a two-dimensional
array of 1-μm diameter holes in a thin chrome film on glass.*

of classical optics [spot size $s = (F / d)\lambda$, where F is the focal length of the lens, d is lens diameter, and λ is the wavelength of the ultrasonic waves]. An example of this type of image is shown in Fig. 9(a). The object shown is a two-dimensional array of 1-μm holes in a chrome thin film deposited on a glass substrate. For comparison, a SEM (scanning electron microscope) image of a similar area on the same object is shown in Fig. 9(b). Note the fine surface details visible in the acoustic image that are not visible in the SEM image. The superiority of the cryogenic acoustic microscope at disclosing surface details is evident. Even though the SEM has superior theoretical resolution, it is not a good choice for imaging the relatively flat surfaces and thin films that occur commonly on modern electronic devices. Resolution alone is not a sufficient criterion for choosing a high-resolution technique. The ability of the imaging instrument to produce contrast between different areas of interest on the object is just as important. The cryogenic acoustic microscope yields high-contrast images because it has a shallow depth of focus (30 nm), which serves to convert height variations in this range to gray levels ranging from black to white. It is also sensitive to the angle of the object's surface relative to the optical axis.

On the other hand, at high input power levels, where propagation through the coupling fluid is non-linear, classical optics cannot be used to predict the resolution. Other investigators have observed higher than the classically predicted resolution in acoustic microscopes that used water, liquid argon, or liquid nitrogen as the coupling fluid. In these experiments the power density was high enough near the focus to cause the converging acoustic beam to be converted to the second harmonic, which has a smaller spot size [4]. Similar resolution enhancement has never been reported for a cryogenic acoustic microscope that uses superfluid helium as the transmission medium. In our acoustic microscope we have observed image degradation in the range where the received signal is not proportional to the input power. The images taken in the oscillatory region of the signal-vs.-input-power curve exhibit degraded resolution compared to those taken in the linear region, as illustrated by comparing Fig. 9(c) with Fig. 9(a) . The area imaged in Fig. 9(c) is the same as that imaged in Fig. 9(a), except that the input power was increased so that the received signal was at one of the peaks in the oscillatory region of the curve shown in Fig. 7. The resolution has obviously been degraded.
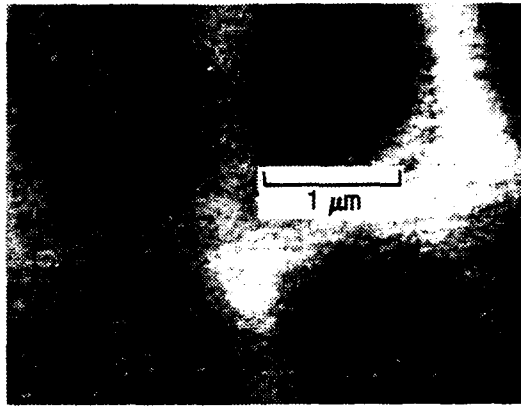
15

Fig. 9(c). *Acoustic image of the same object shown in Fig. 9(a);*
the input power to the transducer was at one of the
peaks in the oscillatory region of the curve shown in
Fig. 7.

16

4. Theoretical Modeling

The adequate modeling of nonlinear effects in focused sound beams began only as recently as the 1950s, with the advent of computers that were capable of handling the numerical solution of the necessary partial differential equations. The earliest models used converging spherical waves but were inadequate in the focal region, since they did not account for diffraction effects [14]. The next step involved the decoupling of nonlinear and diffraction effects, limiting them to the prefocal and focal regions, respectively [15]. However, this failed to account for the complicated behavior of the harmonic components in the focal region, since these two effects indeed interact. Improvement in modeling occurred with quasilinear theory, which covered the combined effects of diffraction and weak nonlinearity and was based on the Fresnel or parabolic approximations [16,17]. With the development of the Khokhlov-Zabolotskaya-Kuznetsov (KZK) parabolic equation [18,19], which accounts for nonlinearity, diffraction, and absorption beyond the usual quasi-linear theory, came a whole set of models for various special cases. For example, Bakhvalov et al. [20] modeled the weak diffraction and low-focusing-gain regime; the lossless case was dealt with by Zabolotskaya and Khokhlov [21]; moderately focused beams were addressed by Baker et al.[22]; and because of their amenability to mathematical analysis, focused Gaussian beams were investigated by others [23].

Our attempt to model the experimentally observed nonlinear phenomenon will be based on the works of several investigators. (1) Tjøtta and Tjøtta [24] and Aanonsen, Barkve, Tjøtta, and Tjøtta [25] modeled the propagation and interaction of finite-amplitude (nonfocused) sound waves in a thermoviscous liquid by means of the KZK equation. (2) Hart and Hamilton [26] employed a convergent coordinate system that improves the efficiency of the numerical solution of the KZK equation for focused beams. (3) Lucas and Muir [27] developed an equivalency relationship, useful in the initial condition formulation for the KZK equation, between a concave spherical source and a planar source. (4) Berntsen and Vefring [28] made detailed evaluations of the numerical algorithms needed to accomplish a spectral solution of the KZK equation. The problem we address, unlike those already studied, is that the following conditions apply simultaneously: (1) There is large focusing gain, (2) the aperture angle is relatively large (so that the so-called Fresnel approximation is invalid), and (3) there is significant pump depletion of the first harmonic of the input acoustic power.

Figure 1 portrays schematically the salient features of the 15.3-GHz acoustic lens that is at the heart of the acoustic microscope. The input signal entering the matching network is taken to be at one frequency, with the amount of power adjustable. The propagating waves in the sapphire rod are assumed to be planar, and are focused onto the object by a simple spherical refracting surface. These focused waves are reflected back up into the lens assembly and the fundamental of the returned signal is detected and its power measured. The focused and reflected waves propagate through superfluid helium at an ambient temperature of $\theta_0 = 0.5$ K and pressure of $p_e = 20$ bar. The measured output fundamental power versus the input fundamental power is shown in Fig. 7 and has already been discussed above. It is this behavior that we wish to model mathematically.

Assuming there is little interaction between the incoming waves and the reflected ones, we can think of the former as passing through the focal region and impinging on an imaginary receiver on the other side of the object. This leads to a geometric model (depicted in Fig. 10) that is axially symmetric about the z-axis. Here r represents a positive radial coordinate, making the overall coordinate system essentially cylindrical. The corresponding dimensionless scaled coordinates σ and u, defined as

17
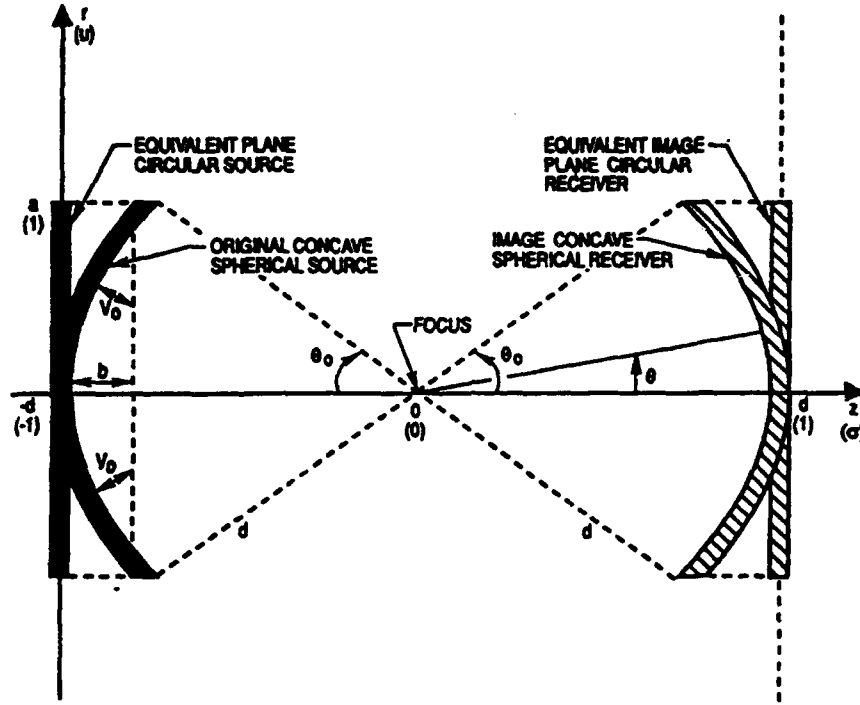
Fig. 10. Geometric model used for the acoustic microscope, depicting the relevant parameters and defining the coordinate systems employed in our analysis. From the experimental apparatus, we have the measured values of a = 0.135 mm, b = 0.051 mm, d = 0.203 mm, and $\theta_0 = 41.4^o$.

$$\sigma := \frac{z}{d} \text{ and } u := \frac{r}{a} \tag{1}$$

will be used in our mathematical model below. The model is seen to consist of the following important elements:

(i) One concave spherical source of curvature radius d, base diameter $2a$, segment height b, and aperture angle θ_0, and located at $z = -d$, represents the sapphire spherical lens. It is readily shown that the following relationships hold between the lens parameters:

$$a = \sqrt{b(2d-b)} \text{ and } \theta_0 = \sin^{-1}\left(\frac{a}{d}\right) \tag{2}$$

The values for the experimental apparatus are included in the caption of Fig. 10. In view of the one-tone input signal, we assume that the source surface oscillates sinusoidally and uniformly normal to itself with a velocity amplitude of v_0.

18

(ii)Tangent to the source in (i) is an equivalent planar source of radius a located at $z = -d$. The particulars of this transformation will be detailed below.

(iii) The images of the two sources just described are reflected through the focus ($z = 0$); the images are located at $z = +d$, and represent the receiver portion of our model. Of course, we assume here that the superfluid helium extends from $z = -d$ to $+d$, where the waves propagate.

As a first attempt at modeling the observed behavior mathematically, we employ the well-known KZK equation, which is derived from the standard Navier-Stokes (N-S) hydrodynamics equations (viz. [25] and [26]). This is justified by the ability of the KZK equation to take into account moderate nonlinearities, diffraction, and absorption in sound beams of significant amplitude, as in our case, where the usual quasi-linear approaches are rendered inapplicable. We begin with a dimensionless form of the KZK equation found in [27] and apply it to our axially symmetric context, namely,

$$\left(\frac{\partial^2}{\partial \tau \partial \sigma} - \frac{1}{4G} \nabla_\perp^2 - A \frac{\partial^3}{\partial \tau^3} \right) P(\sigma, u, \tau) = \frac{B}{2} \frac{\partial^2}{\partial \tau^2} [P^2(\sigma, u, \tau)] \tag{3}$$

where the following hold:

(i) u and σ are the dimensionless transverse and axial coordinates, respectively, defined in Eq. (1), while

$$\tau := \omega \left(t - \frac{z}{c_0} \right) \tag{4a}$$

is a dimensionless retarded time, where

$$f \approx \frac{\omega}{2\pi} \tag{4b}$$

is the source frequency (15.3 GHz) and c_0 is the ambient sound speed (336 m/s).

(ii) P is the dimensionless normalized deviation of the acoustic pressure p from its equilibrium value and is given by

$$P(\sigma, u, \tau) := \frac{p(\sigma, u, \tau) - p_e}{p_0} \tag{5}$$

where p_e is the ambient acoustic pressure (20 bar) and p_0 is the pressure amplitude at the lens.

(iii) $\nabla_\perp^2$ is the transverse portion of the usual Laplacian operator in cylindrical coordinates, assuming axisymmetry (that is, there is no dependence on the polar angle φ). Hence

$$\nabla_{\perp}^2 = \frac{\partial^2}{\partial u^2} + \frac{1}{u}\left(\frac{\partial}{\partial u}\right) \tag{6}$$

(iv) A is the dimensionless absorption given by

$$A = \alpha d \tag{7a}$$

where

$$\alpha = \frac{D\omega^2}{2c_0^3} \tag{7b}$$

is the thermoviscous attenuation coefficient, and

$$D = \left(\frac{\frac{4}{3}\mu_0 + \kappa_0}{\rho_0}\right) + \left(\frac{\gamma-1}{\gamma}\right)K_0 \tag{7c}$$

is the sound diffusivity, where μ_0, κ_0, and K_0 are the ambient values of the coefficients of shear viscosity, bulk viscosity, and thermal conductivity, respectively; ρ_0 is the ambient mass density; and γ is the ratio of specific heat at constant pressure c_p to the specific heat at constant volume c_v. In our case D is very small, since μ_0 and κ_0 are much smaller than ρ_0 (0.18 gm/cm^3) and γ is nearly unity with K_0 approximately equal to 10^{-2} W/cm-K. For now, we will be taking A to be a constant with a value between 0.01 to 0.1.

(v) B is the dimensionless source amplitude given by

$$B = \frac{d}{l_p} \tag{8a}$$

where

$$l_p = \frac{\rho_0 c_0^3}{\beta \omega p_0} \tag{8b}$$

is the plane-wave shock formation distance ($\sim 10^{-4}$ m at the source and ~ 10 nm at the focal plane), and

$$\beta = 1 + \frac{\rho_0}{c_0}\left(\frac{dc}{d\rho}\right)_0 \tag{8c}$$

20

is the coefficient of nonlinearity, where c is the isentropic speed of sound whose ambient value is c_0. We will vary the value of B over the range 0.1 to 1,000, reflecting the variation of the input signal's power.

(vi) G is the linear focusing gain given by

$$G = \frac{z_0}{d} \qquad (9a)$$

where

$$z_0 = \frac{\omega a^2}{2c_0} \qquad (9b)$$

is the Rayleigh distance of the unfocused source. In our case, G is approximately 1.27×10^4, a much larger value than the one used in [27].

The assumptions under which the KZK equation is derived from the N-S hydrodynamic equations are summarized and discussed in our context below:

Assumption 1. The shear (μ) and bulk (κ) viscosities are very small and essentially spatially constant. This is true, from experimental measurement, for liquids, and for liquid He in particular.

Assumption 2. The fluid is homogeneous and irrotational in its flow, the latter meaning that for all space and time,

$$\nabla \times \mathbf{v} \equiv 0 \qquad (10)$$

where $\mathbf{v} = \mathbf{v}(\sigma, u, \tau)$ is the velocity field of the flow. This is justified by the purity of the liquid He and because no agitation is occurring in our experimental setup.

Assumption 3. Viscosity terms have been linearized in the N-S force equation, while viscosity, heat-conduction, and relaxation terms have been linearized in the N-S heat-exchange equation. Terms of cubic or higher order in the acoustic variables are ignored. These approximations are adequate for our situation, since even the linear terms are small, and the higher-order terms will be smaller.

Assumption 4. The temperature is essentially constant in space and time, so that

$$\Theta(\sigma, u, \tau) \equiv \Theta_0 = 0.5 \, K \qquad (11)$$

This assumption holds well for liquid He, which experimentally satisfies the isothermal condition

$$\frac{2K_0}{c_0 \rho_0 c_v} \gg \lambda = \frac{c_0}{f} \qquad (12)$$

21

In fact, in our case the left-hand quantity in Eq. (12) is about 1.32×10^{-4} cm, whereas $\lambda = 2.20 \times 10^{-6}$ cm.

Assumption 5. The parabolic approximation, a standard one used in optics, holds. In our context, this means that the second partial derivative along the axis of propagation, that is, along the positive z direction, is neglected. Equivalently, this means that the amplitude of the pressure wave does not change very much along its direction of propagation within a distance of one wavelength. Again, we tentatively assume the validity of this approximation, although it may not be valid in the focal region.

In order to facilitate the numerical solution of Eq. (3), we make the transformation introduced in [27], following the convergent geometry of the focused beam:

$$\left.\begin{array}{l} \overline{P}(\sigma, \overline{u}, \overline{\tau}) := (\sigma \pm \delta) P(\sigma, u, \tau) \Rightarrow P = \dfrac{\overline{P}}{(\sigma \pm \delta)} \\[2ex] \overline{u} := \dfrac{u}{|\sigma \pm \delta|} \Rightarrow u = |\sigma \pm \delta| \overline{u} \\[2ex] \overline{\tau} := \tau - \dfrac{Gu^2}{(\sigma \pm \delta)} \Rightarrow \tau = \overline{\tau} + G(\sigma \pm \delta) u^2 \end{array}\right\} \tag{13}$$

where δ is a small positive quantity that governs the rate at which the transformed geometry converges ($\delta \approx 0.01$ for our case), and the plus (or minus) sign in front of δ holds for the postfocal (or prefocal) region, that is, for $\sigma > 0$ (or < 0). Observe from the second relation in Eq. (13) that for $\delta \ll 1$, the axial length scale at the focal plane ($\sigma = 0$) is δ times smaller than at the source ($\sigma = -1$). Applying Eq. (13) to Eq. (3) readily leads to

$$\left[(\sigma \pm \delta)^2 \frac{\partial^2}{\partial \overline{\tau} \partial \sigma} - \frac{1}{4G} \overline{\nabla}_\perp^2 - (\sigma \pm \delta)^2 A \frac{\partial^3}{\partial \overline{\tau}^3} \right] \overline{P} = (\sigma \pm \delta) \frac{B}{2} \frac{\partial^2 (\overline{P}^2)}{\partial \overline{\tau}^2} \tag{14a}$$

where

$$\overline{P} = \overline{P}(\sigma, \overline{u}, \overline{\tau}) \tag{14b}$$

and

$$\overline{\nabla}_\perp^2 = \frac{\partial^2}{\partial \overline{u}^2} + \frac{1}{\overline{u}} \left(\frac{\partial}{\partial \overline{u}} \right) \tag{14c}$$

is the transverse component of the Laplacian operator for an axisymmetric sound field in the new coordinate system.

Now we solve Eq. (14a) by applying the spectral method. Assume that $\overline{P}$ in Eq. (14b) can be expanded into a complex Fourier series in $\overline{\tau}$ with a basic period 2π:

$$\overline{P}(\sigma,\overline{u},\overline{\tau}) = \sum_{\substack{n=-\infty \\ (n\neq 0)}}^{\infty} \overline{p}_n(\sigma,\overline{u}) e^{jn\overline{\tau}} \qquad (15)$$

where $\overline{p}_n$ is the complex Fourier component of $\overline{P}$ at the frequency $\omega_n = n \in \mathbf{Z} \setminus \{0\}$ that satisfies

$$\overline{p}_{-n}(\sigma,\overline{u}) \equiv \overline{p}_n^*(\sigma,\overline{u}) \forall n \in \mathbf{N} \qquad (16)$$

since $\overline{P}$ is real. We leave out the zero frequency in Eq. (15), using Eq. (5) and the fact that p oscillates about p_e. If we write

$$\overline{p}_n(\sigma,\overline{u}) =: \overline{p}_{nr}(\sigma,\overline{u}) + j\,\overline{p}_{ni}(\sigma,\overline{u}), n \in \mathbf{N} \qquad (17)$$

where $\overline{p}_{nr}$ and $\overline{p}_{ni}$ are real-valued functions of σ and $\overline{u}$, Eq. (15) can be reexpressed as

$$\overline{P}(\sigma,\overline{u},\overline{\tau}) = 2\sum_{n=1}^{\infty} [\overline{p}_{nr}(\sigma,\overline{u}) \cos n\overline{\tau} - \overline{p}_{ni}(\sigma,\overline{u}) \sin n\overline{\tau}] \qquad (18)$$

Substituting Eq. (18) into Eq. (14) and limiting the number of harmonics to a finite number (which is seen as an approximation of $\overline{P}$ by a finite real Fourier series), we arrive at the following coupled system of $2N$ second-order quasi-linear parabolic partial differential equations:

$$\frac{\partial \overline{p}_{nr}}{\partial \sigma} = -n^2 A\,\overline{p}_{nr} + \frac{1}{4nG(\sigma \pm \delta)^2} \overline{\nabla}_{\perp}^2 \overline{p}_{ni} - \frac{nB}{2(\sigma \pm \delta)}$$
$$\left[(1-\delta_{n-1})\sum_{m=1}^{n-1} (\overline{p}_{mr}\overline{p}_{n-m,i} + \overline{p}_{mi}\overline{p}_{n-m,r} + 2(1-\delta_{n-N}) \sum_{m=n+1}^{N} (\overline{p}_{mi}\overline{p}_{m-n,r} - \overline{p}_{mr}\overline{p}_{m-n,i}) \right], \qquad (19a)$$
$$n = 1,...,N$$

$$\frac{\partial \overline{p}_{ni}}{\partial \sigma} = -n^2 A\,\overline{p}_{ni} - \frac{1}{4nG(\sigma \pm \delta)^2} \overline{\nabla}_{\perp}^2 \overline{p}_{nr} + \frac{nB}{2(\sigma \pm \delta)}$$
$$\left[(1-\delta_{n-1})\sum_{m=1}^{n-1} (\overline{p}_{mr}\overline{p}_{n-m,r} - \overline{p}_{mi}\overline{p}_{n-m,i} + 2(1-\delta_{n-N}) \sum_{m=n+1}^{N} (\overline{p}_{mr}\overline{p}_{m-n,r} + \overline{p}_{mi}\overline{p}_{m-n,i}) \right], \qquad (19b)$$
$$n = 1,...,N$$

where

$$\overline{p}_{lr} = \overline{p}_{lr}(\sigma,\overline{u}), \overline{p}_{li} = \overline{p}_{li}(\sigma,\overline{u}), l = 1,...,N \qquad (19c)$$

and

$$\delta_{n-1}(\delta_{n-N}) := \begin{cases} 1 & \text{if } n = 1(N) \\ 0 & \text{if } n \neq 1(N) \end{cases} \tag{19d}$$

is a Kronecker delta function in the variable $n - 1(n - N)$.

In order to solve Eq. (19), we need to specify the initial conditions for the source and to provide the necessary boundary conditions. For the first task, we use the technique discussed in Appendix A of [28] to replace the actual concave source with an equivalent planar circular one so that the same radiation field is produced. The planar source will be a piston of radius a that is phase modulated in a perfectly compliant baffle. This is a good approximation, provided that

$$ka = \frac{\omega a}{c_0} \gg 1 \tag{20}$$

which holds very well in our case, since $ka = 3.86 \times 10^4$. Proceeding in a manner similar to that of [28], performing the necessary set of coordinate transformations [that is, Eqs. (1), (4a), (5), and (13)], assuming that the linear impedance relation

$$p_0 = \rho_0 c_0 v_0 \tag{21}$$

holds, using the fact that

$$kd = 5.81 \times 10^4 \gg 1 \tag{22}$$

is satisfied in our case, and then making the appropriate Fourier series expansion, we straightforwardly arrive at the following initial conditions for $\bar{p}_{nr}$ and $\bar{p}_{ni}$ at $\sigma = -1$ (the position of the equivalent plane source), $n = 1, \dots, N$:

$$\left. \begin{array}{l} \bar{p}_{lr}(\sigma = -1, \bar{u}) = +\beta(\bar{u}) \cos \psi(\bar{u}) \\ \bar{p}_{li}(\sigma = -1, \bar{u}) = -\beta(\bar{u}) \sin \psi(\bar{u}) \end{array} \right\} \text{ for } 0 \leq \bar{u} \leq \tfrac{1}{\gamma} \tag{23a}$$

$$\bar{p}_{lr}(\sigma = -1, \bar{u}) \equiv 0, \bar{p}_{li}(\sigma = -1, \bar{u}) \equiv 0, \text{ for } \bar{u} > \tfrac{1}{\gamma} \tag{23b}$$

$$\bar{p}_{nr}(\sigma = -1, \bar{u}) \equiv 0, \bar{p}_{ni}(\sigma = -1, \bar{u}) \equiv 0, n = 2, \dots, N \text{ for } \bar{u} \geq 0 \tag{23c}$$

where

$$\beta(\bar{u}) := \frac{\gamma}{\varphi(\bar{v})} \qquad (24a)$$

$$\psi(\bar{u}) := kd\left[\varphi(\bar{v}) + \tfrac{1}{2}\left(\tfrac{a}{d}\right)^2 \bar{u}^2\right] \qquad (24b)$$

and

$$\psi(\bar{u}) := 2\sqrt{1 + \left(\frac{a}{d}\right)^2 (\gamma\bar{u})^2} \qquad (24c)$$

$$\gamma := 1 + \delta \qquad (24d)$$

For the boundary conditions, we limit the region in $\bar{u}$ as in [27] to

$$0 \le \bar{u} \le \bar{u}_{max} \qquad (25a)$$

where for high focusing gain (as we have here)

$$\bar{u}_{max} := \tfrac{1.1}{\gamma} > \tfrac{1}{\gamma} \qquad (25b)$$

and impose for $n = 1,..., N$, and all $\sigma \ge -1$ the following mixed conditions:

$$\bar{p}_{nr}(\sigma,\bar{u}_{max}) = 0, \bar{p}_{ni}(\sigma,\bar{u}_{max}) = 0, \frac{\partial \bar{p}_{nr}(\sigma,\bar{u}=0)}{\partial \bar{u}} = 0, \frac{\partial \bar{p}_{ni}(\sigma,\bar{u}=0)}{\partial \bar{u}} = 0 \qquad (26)$$

The latter two Neumann-type constraints are a result of the axisymmetry in our model, while the former two Dirichlet-type requirements are seen to be continuous with the initial conditions in Eq. (23) at $\sigma = -1$, $\bar{u} = \bar{u}_{max}$ in view of Eq. (25b).

Once we have obtained $\bar{p}_{nr}(\sigma,\bar{u})$ and $\bar{p}_{ni}(\sigma,\bar{u})$ from Eq. (19) with the conditions in Eqs. (23) and (26) (see discussion below), we calculate $\bar{p}_n(\sigma,\bar{u})$ by means of Eq. (17) and then $p_n(\sigma,\bar{u})$, the corresponding complex Fourier coefficient of $P(\sigma,u,\tau)$ that we need for our power calculations, using the easily demonstrated relation

$$p_n(\sigma,u) = \frac{\exp\left[-jn\left(\dfrac{Gu^2}{\sigma \pm \delta}\right)\right]}{\sigma \pm \delta} \bar{p}_n\left(\sigma, \frac{u}{|\sigma \pm \delta|}\right), n = 1,...,N \qquad (27a)$$

and the usual symmetry relation

$$p_{-n}(\sigma,u) \equiv p_n^*(\sigma,u), n = 1,...,N \qquad (27b)$$

25

We seek the relationship between the first-harmonic input radiated power P_i^1 from the spherical cap source and the first-harmonic received power P_r^1 at the spherical cap receiver (see Fig. 10). Observe that this relationship is qualitatively identical to the one between

$$Q_i^1(p_0) := p_0^2 |\int_{source} p_1(\sigma,u)dS|^2 \qquad (28a)$$

and

$$Q_r^1(p_0) := p_0^2 |\int_{receiver} p_1(\sigma,u)dS|^2 \qquad (28b)$$

using Eq. (5) and noting that the square of the perturbation of the acoustic pressure from its equilibrium value is related to the perturbation intensity, which, when integrated, corresponds to the radiated power measured. From the nature of our source and its equivalent, $Q_r^1(p_0)$ will vary linearly with p_0^2 (which is used to make our power sweep of the input signal). On the other hand, the absolutely squared quantity in $Q_r^1(p_0)$ will be a function of p_0 through the source amplitude B in Eq. (19) that produces $p_1(\sigma,u)$ [see Eq. (8)]. Using Eq. (27) and the geometry provided in Fig. 10, we can straightforwardly elaborate Eq. (28b) to the desired state of

$$Q_r^1(p_0)\, 4\pi^2 p_0^2 d^4 \left\{ \left[\int_0^{\theta_0} d\theta \left(\frac{\bar{p}_{1r}\cos\eta(\theta) + \bar{p}_{1i}\sin\eta(\theta)}{\delta + \cos\theta} \right)\sin\theta \right]^2 + \left[\int_0^{\theta_0} d\theta \left(\frac{\bar{p}_{1i}\cos\eta(\theta) - \bar{p}_{1r}\sin\eta(\theta)}{\delta + \cos\theta} \right)\cos\theta \right]^2 \right\} \qquad (29a)$$

where

$$\eta(\theta) := \frac{Gd^2 \sin^2\theta}{(\delta + \cos\theta)a^2} + \frac{\omega d \cos\theta}{c_0} \qquad (29b)$$

and

$$\bar{p}_{1r} = \bar{p}_{1r}\left(\cos\theta, \frac{d\sin\theta}{a(\delta + \cos\theta)}\right), \quad \bar{p}_{1i} = \bar{p}_{1i}\left(\cos\theta, \frac{d\sin\theta}{a(\delta + \cos\theta)}\right) \qquad (29c)$$

In view of what was said about $Q_i^1(p_0)$ above, it follows that a plot of $Q_r^1(p_0)$ vs. p_0^2 would be our model for the observed power phenomena.

Our progress towards the modeling of the harmonic power exchange in the cryogenic acoustic microscope is at a stage where we are about to solve numerically the partial differential equation system Eq. (19) under the conditions of Eqs. (23) and (26). Note that we must solve the complete set of equations because of the coupling between harmonics, even though we only need $\bar{p}_{1r}$ and $\bar{p}_{1i}$ in Eq. (29). Employing [26] as a guide, we choose the number of harmonics to retain in Eq. (18)

26

to be $N = 10$ and note that this should not lead to too much truncation error, since our Gol'dberg number Γ is given by

$$\Gamma := (\alpha l_p)^{-1} \approx 10 - 100 \qquad (30)$$

and hence is not too large. We propose to do our numerical solution with the CRAY Mathlib routine RKFPDE, which uses the method of lines (as opposed to the implicit methods studied in [29], which were not readily available in software form). In our context, this technique approximates the Laplacian operator in Eq. (19) by differences, and the resulting larger system of ordinary differential equations is integrated using the standard RKF routine (with σ thought of as a time variable). Our future goals include carrying out the aforementioned procedure, using the results in the numerical integration in Eq. (29), or possibly its equivalent involving the planar image receiver at $\sigma = +1$ instead, and then comparing the plot of $Q_r^1(p_0)$ vs. p_0^2 with the experimentally derived plot (that is, Fig. 7). Depending upon the accuracy of our model, we may then have to proceed with the appropriate modifications and refinements. Our findings will be reported later.

References

1. J. S. Foster and D. Rugar, "High resolution acoustic microscopy in superfluid helium," *Appl. Phys. Lett.*, vol. 42, no. 10, pp. 869-871 (May 1983).

2. B. Hadimioglu and J. S. Foster, "Advances in superfluid helium acoustic microscopy," *J. Appl.Phys.*, vol. 56,no. 7, pp. 1976-1980 (Oct. 1984).

3. K. Karaki, M. Suzuki, Y. Okuda, "Acoustic microscope using pressurized superfluid ^{4}He," *J. Appl. Phys.*, vol. 67, no. 4, pp.1680-1683 (Feb. 1990).

4. D. Rugar, "Resolution beyond the diffraction limit in the acoustic microscope: A nonlinear effect," *J. Appl. Phys.*, vol. 56, no. 5, pp. 1338-1346 (Sept. 1984).

5. D. R. Wright, B. Hadimioglu, L. J. LaComb, Jr., C. F. Quate, J. S. Foster, "Observation of the pressure dependence of nonlinear interactions in a focused coherent acoustic beam in superfluid helium," *Japanese J. Appl. Phys.*, vol. 26, suppl. 26-3, pp. 9-10 (1987).

6. B. Hadimioglu, L. J. LaComb, Jr., D. R. Wright, B. T. Khuri-Yakub, and C. F. Quate, "High efficiency, multiple layer ZnO acoustic transducers at millimeter-wave frequencies," *Appl. Phys. Lett.*, vol. 50, no. 23, pp. 1642-1644 (June 1987).

7. F. E. Scire and E. C. Teague, "Piezodriven 50-μm range stage with subnanometer resolution," *Rev. Sci. Instrum.*, vol. 49, no. 12, pp. 1735-1740 (Dec. 1978).

8. Harmonic Drive Division, Emhart Machinery Group, 51 Armory Street, Wakefield, MA 01880.

9. A. A. Moulthrop and M. S. Muha, "Superconducting stepper motors," *Rev. Sci. Instrum.*, vol. 59, no. 4, pp. 649-650 (April 1988).

10. Supercon, Inc., 830 Boston Turnpike, Shrewsbury, MA 01545.

11. Micro Coax Components, Inc., Box E, 245 West 5th Avenue, Collegeville, PA 19426.

12. Wiltron Co., 490 Jarvis Drive, Morgan Hill, CA 95037-2809.

13. R. K. Pathria, *Statistical Mechanics* (Oxford: Pergamon, 1972), p. 206.

14. K. A. Naugol'nykh, S. I. Soluyan, and R. V. Khokhlov, "Spherical Waves of Finite Amplitude in a Viscous Thermally Conducting Medium," *Sov. Phys. Acoust.*, vol. 9, pp. 42-46 (1963).

15. L. A. Ostrovskii and A. M. Sutin, "Focusing of Finite-Amplitude Acoustic Waves," *Sov. Phys. Dokl.*, vol. 20, pp. 275-277 (1975).

16. B. G. Lucas and T. G. Muir, "The Field of a Finite-Amplitude Focusing Source," *J. Acoust. Soc. Am.*, vol. 74, no. 5, pp. 1522-1528 (Nov. 1983).

17. S. Saito, B. C. Kim, and T. G. Muir, "Second Harmonic Component of a Nonlinearly Distorted Wave in a cused Sound Field," *J. Acoust. Soc. Am.*, vol. 82, no. 2, pp. 621-628 (Aug. 1987).

18. V. P. Kuznetsov, "Equations of Nonlinear Acoustics," *Sov. Phys. Acoust.*, vol. 16, no. 4, pp. 467-470 (April-June 1971).

19. E. A. Zabolotskaya and R. V. Khokhlov, "Quasiplane Waves in the Nonlinear Acoustics of Confined Beams," *Sov. Phys. Acoust.*, vol. 15, no. 1, pp. 35-40 (July-Sept. 1969).

20. N. S. Bakhvalov, Ya. M. Zhileikin, and E. A. Zabolotskaya, *Nonlinear Theory of Sound Beams* (New York: American Institute of Physics, 1987).

21. E. A. Zabolotskaya and R. V. Khokhlov, "Convergent and Divergent Sound Beams in Nonlinear Media," *Sov. Phys. Acoust.*, vol. 16, no. 1, pp. 39-42 (July-Sept 1970).

22. A. C. Baker, K. Anastasiadis, and V. F. Humphrey, "Nonlinear Propagation in Focused Fields: Experiment and Theory," in *Proceedings of Ultrasonics International, London*, pp. 184-189 (July 1987).

23. G. Du and M. A. Breazeale, "Theoretical Description of a Focused Gaussian Ultrasonic Beam in a Nonlinear Medium," *J. Acoust. Soc. Am.*, vol. 81, no. 1, pp. 51-57 (Jan. 1987).

24. J. N. Tjøtta and J. S. Tjøtta, "Nonlinear Equations of Acoustics, with Applications to Parametric Acoustic Arrays," *J. Acoust. Soc. Am.*, vol. 69, no. 6, pp. 1644-1652 (June 1981).

25. S. I. Aanonsen, T. Barkve, J. N. Tjøtta, and J. S. Tjøtta, "Distortion and Harmonic Generation in the Nearfield of a Finite Amplitude Sound Beam," *J. Acoust. Soc. Am.*, vol. 75, no. 3, pp. 749-768 (March 1984).

26. T. S. Hart and M. F. Hamilton, "Nonlinear Effects in Focused Sound Beams," *J. Acoust. Soc. Am.*, vol. 84, no. 4, pp. 1488-1496 (Oct. 1988).

27. B. G. Lucas and T. G. Muir, "The Field of a Focusing Source," *J. Acoust. Soc. Am.*, vol. 72, no. 4, pp. 1289-1296 (Oct. 1982).

28. J. Berntsen and E. Vefring, "Numerical Computation of a Finite Amplitude Sound Beam," Report no. 81, Dept. of Mathematics, University of Bergen, Bergen, Norway (Nov. 1986).

30